Available online at www.sciencedirect.com
ScienceDirect
C. R. Physique 10 (2009) 197–206
COMPTES RENDUS PHYSIQUE

Laser acceleration of particles in plasmas / Accélération laser de particules dans les plasmas

Ion acceleration with high-intensity lasers and application to isochoric heating

Erik Lefebvre *, Michaël Carrié, Rachel Nuter

CEA, DAM, DIF, Bruyères-le-Châtel, 91297 Arpajon cedex, France

Available online 28 April 2009

Abstract

Very nonlinear mechanisms are at play in the acceleration of ions with high-intensity laser pulses, and the properties of the resulting particle beams depend on many parameters. We first explore, in this article, the dependence on the target density profile and on the laser pulse duration. We next show numerically that using targets on which thin, low-density proton layers are deposited, it should be possible to produce proton beams suitable for heating a solid aluminum target to the GJ/kg level over a depth of several micrometers. ***To cite this article: E. Lefebvre et al., C. R. Physique 10 (2009).***

Résumé

Accélération ionique par laser ultra-intense et application au chauffage isochore. L'accélération d'ions à l'aide d'impulsions laser ultra-intenses met en jeu une physique complexe, et les propriétés des faisceaux de particules produits dépendent de nombreux paramètres. Nous explorons tout d'abord dans cet article les dépendances avec le profil de densité de la cible et la durée de l'impulsion laser. Dans un second temps, nous montrons à l'aide de simulations numériques qu'il devrait être possible, en utilisant des cibles sur lesquelles sont déposées des couches minces et peu denses de protons, d'accélérer un faisceau d'ions susceptible de chauffer une cible d'aluminium jusqu'à 1 GJ/kg sur une profondeur de plusieurs micromètres. ***Pour citer cet article : E. Lefebvre et al., C. R. Physique 10 (2009).***

Keywords: Ion acceleration; Ultrahigh-intensity lasers; Isochoric heating

Mots-clés : Accélération ionique ; Laser ultra-intense ; Chauffage isochore

1. Introduction

In the last decades, improvements in the laser Chirped Pulse Amplification technology have allowed the construction of powerful laser facilities able to deliver on target focused intensities up to several 10^{21} W/cm^2, or even several 10^{22} W/cm^2 [1]. These intense laser pulses can be used to efficiently accelerate high quality proton or ion beams off the rear surface of thin, solid targets. These particle beams are laminar [2], collimated [3] and with μm virtual source

* Corresponding author.
E-mail address: erik.lefebvre@cea.fr (E. Lefebvre).

1631-0705/$ – see front matter
doi:10.1016/j.crhy.2009.03.005

size, and the maximum particle energy can reach several tens of MeV per nucleon. They can be used in a wide range of applications such as imaging in plasma physics [4], the production of warm dense matter [5], or in the medical field with proton therapy [6].

Compared to heating with intense electron beams, protons could offer an interesting alternative for the production of warm dense matter, or even to reach ignition condition in compressed thermonuclear fuel [7]. Indeed, for a similar kinetic energy flux, a proton beam transports less current with heavier particles, and is therefore less affected by nonlinear, self-generated electromagnetic fields. For a given incident particle kinetic energy, the stopping power of ions is also larger than that of electrons, enabling more localized deposition and heating. Finally, some indications of control have been demonstrated with proton and carbon beams, such as focusing [5] and energy selection [8–10]. Alternative schemes to produce monoenergetic ion distributions have been proposed, based on numerical simulations and theory [11,12], but still await experimental confirmation. All these methods could be used for optimal control of energy deposition in a secondary target. Yet even though proton acceleration with intense lasers has been the subject of much interest recently, only a limited number of experimental results have been published regarding proton-induced isochoric heating [5,13–15].

Optimization of ion acceleration is often considered from the point of view of increased energy or larger coupling efficiency from laser light to ion kinetic energy. Other source properties also have to be optimized with respect to specific applications. For isotope production, for instance, spectral quality of the proton beam is of lesser importance than efficiency of the laser-to-ion coupling [16]. For application to isochoric heating, two goals can be pursued. For the first one, one will look for the highest energy deposition into the material of interest; this can be achieved, for instance, by focusing the accelerated ion beam [5], or by using low-energy ions that will deposit their energy in a thinner layer of matter [13]. The other option for optimization might be to look for the largest heated region, and with the most uniform energy deposition across the heated zone, both along its longitudinal and transverse dimensions, in order to ease the observation of the heated medium dynamics, and its interpretation. For a finite laser energy, these two options are likely exclusive.

In this article, we will first report on some source optimization studies that we performed to try and identify the main trends of peak ion energy variations with parameters such as target density profile [17] and laser pulse duration [18]. A straightforward path towards uniform energy deposition is obviously to use controlled proton spectra and rely on the specific properties of proton stopping power through solid matter. In the second half of this article, we will report on some numerical exploratory studies towards this goal.

2. Dependence of acceleration on target density profile

A question of interest in studies of proton acceleration is the optimization of particle energy for a fixed incident laser energy. Proton acceleration is known to depend on both the mean energy and number of hot electrons that can be produced by laser absorption in the target. Controlling the plasma density gradient at the laser-irradiated surface can be one way to control the laser-to-hot electron conversion fraction, as well as the hot electron temperature [19]. This plasma density control can be achieved with an auxiliary, low-intensity heating beam hitting the target prior to the main, high-intensity pulse. In the following section, we study the possibilities offered by such a two-pulse configuration.

2.1. Numerical setup

In our numerical experiments, we consider a 500 nm-thick Al target with a variable density gradient on its laser-irradiated surface, such as could be produced by a low-intensity pulse hitting this target with a variable delay, Δt, before the high-intensity pulse. The interaction of the high-intensity pulse with the Al target was then simulated in two-dimensional (2D) geometry with the CALDER PIC code [20]. The initial plasma density profiles are plotted in Fig. 1a). They were computed with the 1D Lagrangian hydrodynamics code ESTHER [21] for a low-intensity pulse of 150 fs duration, focused to 1.1×10^{16} W/cm^2. After 12 ps, the shock wave launched by the low-intensity pulse breaks out at the rear surface, and likely perturbs proton acceleration [22]. We did not therefore consider delays larger than 15 ps. Due to computational constraints with the PIC simulations, we have imposed lower and upper bounds on the density profiles, equal to $n_c/175$ and $50\,n_c$, respectively ($n_c = 1.74 \times 10^{21}$ cm^{-3} is the critical density at the laser wavelength $\lambda_0 = 0.8$ μm).

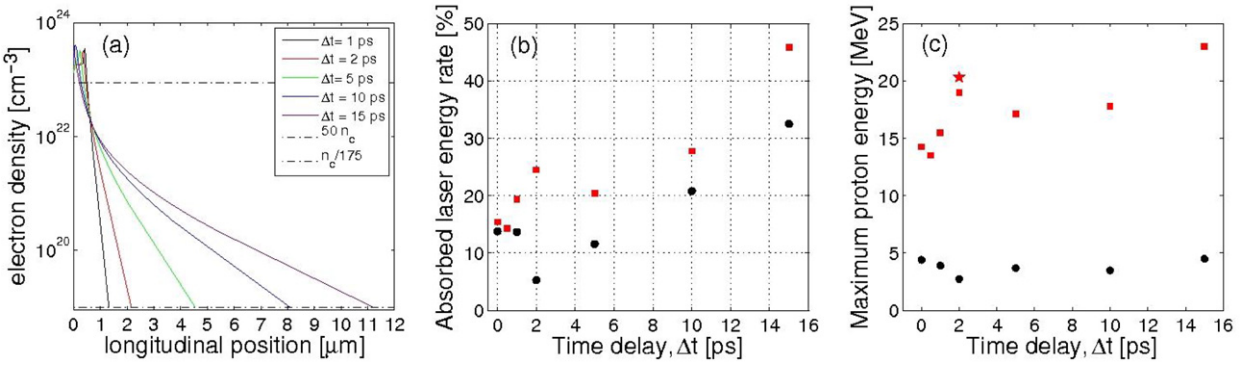

Fig. 1. (a) Electron density profiles at the target irradiated surface for different time delays. The dot-dashed lines represent the lower and upper density bounds considered in PIC simulations. (b) Absorption rate versus the time delay for $E_{\text{in}} = 256$ mJ (squares) and $E_{\text{in}} = 50$ mJ (circles). $\Delta t = 0$ ps denotes the solid target without preplasma. (c) Maximum proton kinetic energy versus time delay for $E_{\text{in}} = 256$ mJ (squares) and $E_{\text{in}} = 50$ mJ (circles).

The electron and ion temperatures are initialized to $T_e = 1$ keV and $T_i = 1$ eV, respectively. The mesh size is set to $\Delta x = \Delta y = 10.12$ nm. To reduce numerical heating down to a low level (<1% of the incident laser energy), 80 particles per cell are used and the current and charge densities are calculated with quadratic weighting factors. Moreover, the numerical box (up to 13 750 × 2176 cells) is chosen sufficiently large to avoid artificial particle absorption at boundaries: its transverse size (22 μm) is larger than three times the focal spot and the longitudinal one (up to 140 μm) is at least equal to 18 times the target thickness. Electrons hitting the box boundaries are reinjected with thermal momentum as long as ions do not reach the boundaries, in which case both species are absorbed to keep the plasma globally neutral. The boundary conditions for the electromagnetic fields are periodic along the y axis and open in the $\pm x$ directions. Finally, a 50 n_c, 20 nm proton layer is put on the Al target rear surface so as to model the ionized hydrogen contaminants.

The fast electrons responsible for ion acceleration are generated by an intense, short duration pulse characterized by two distinct sets of parameters: either a 256 mJ energy, 24 fs duration and a 3.2 μm diameter ($I_0 = 8.6 \times 10^{19}$ W/cm^2), or a 50 mJ energy, 30 fs duration and a 4 μm diameter ($I_0 = 8.6 \times 10^{18}$ W/cm^2). In both cases, the central wavelength is 0.8 μm and the linearly polarized laser beam is normally incident onto the target, with the laser electric field (E_y) in the simulation plane. These laser parameters are typical of current 10-TW, titanium–sapphire laser systems used in many laboratories.

2.2. *Fast electron generation*

We first focus on the electron acceleration mechanisms occurring during the interaction of the ultra-intense laser with the target, whether preceded by a plasma or not.

Fig. 1b) plots the absorbed laser energy as a function of the time delay between the low-intensity and relativistic intensity pulses. Whereas the absorption rate for a steep gradient target ($\Delta t = 0$ ps) is identical for both intense pulses (∼15%), it is seen to increase with laser energy when a large preplasma (corresponding to $\Delta t > 5$ ps and 10 ps for $E_{\text{in}} = 256$ mJ and 50 mJ, respectively) is added in front of the target.

For the shorter delays and steeper plasmas, the two high-intensity pulses show opposing behaviors, with the lower energy (50 mJ) case showing first a decreases and then an increase of absorption for $\Delta t > 2$ ps, whereas the high-energy case exhibits a local maximum around the same delay. This feature suggests that different electron heating mechanisms are at play in the preplasma. When the normally incident, moderate-intensity laser directly interacts with the sharp-gradient target, electrons are mostly heated through the relativistic $\mathbf{j} \times \mathbf{B}$ mechanism [23]. The Lorentz force oscillates the electrons inside the target in the longitudinal direction with its evanescent part mainly oscillating at twice the laser frequency. Electrons are also pulled back towards the plasma surface by the restoring electrostatic fields. Heating results from the crossings of electron trajectories during this complicated motion [24,25]. As a thin preplasma is added in front of the solid target, this process becomes less efficient: the absorption rate decreases down

to 5.3% for $\Delta t = 2$ ps. Indeed, as the preplasma length increases, the evanescent part of the Lorentz force reaches regions of lower electron density and can heat a smaller number of particles.

For the high-energy case, on the other hand, the observed local maximum around $\Delta t = 2$ ps in the absorption rate is reminiscent of a theoretical prediction made by Andreev et al. [26]. According to these authors, this optimal preplasma scale length is that for which the $2\omega_0$-oscillating evanescent part of the Lorentz force is best able to resonantly excite an electrostatic wave in the vicinity of $n_e = 4n_c$, hence enhancing laser absorption. This point is discussed in more detail in another publication [17].

Despite those different trends at short delays, both laser energy cases show a steadily increase of absorption with Δt for $\Delta t > 5$ ps. In this configuration, the preplasma electrons are accelerated by a standing wave resulting from the superposition of the incident and reflected laser pulses. This most efficient heating mechanism can be related to the stochastic heating evidenced so far for longer laser durations [27,28]. Sentoku et al. [29] have shown in this case that the electron kinetic energy and the absorption rate increase with the laser energy and the plasma scale length (l_{ss}), respectively, up to a saturation when $l_{ss} \simeq 10\lambda_0$. In our configuration, the plasma gradient length is always below this threshold value, and we observe a monotonous increase in the electron temperature and the absorption rate with the plasma scale length. Note that for these preplasma parameters, absorption can also be enhanced due to 2D effects originating from the deformation of the irradiated target surface [30]. This leads us to the conclusion that in our configuration, the standing wave heating mechanism is the most efficient to generate hot electrons.

2.3. Proton acceleration

We now plot in Fig. 1c) the cut-off proton energies that result from the laser–foil interaction with various density scale lengths. These energies correspond to saturated values obtained after several picoseconds. First, as expected, the proton cut-off energy increases as the laser energy increases, as already measured [31]. On the whole, the plot of proton maximum energy versus the preplasma length is similar to the absorption curve.

Fig. 1c) shows that for a given laser energy, increasing the proton cut-off energy can be achieved by increasing the plasma scale length. This shows that in the TNSA regime of proton acceleration, a two-pulse configuration (using a low-intensity beam to control the plasma gradient before sending the high-intensity beam onto the target) is able to increase the peak proton kinetic energy. This setup involves the generation of a preplasma in front of the thin foil target in order to enhance the fraction of absorbed laser energy, and a knowledge of the shock wave propagation to determine the maximum time delay at which the relativistic laser beam should be focused on target.

We have observed that the electron heating mechanisms occurring during the laser–plasma interaction depend on both the laser intensity and the plasma characteristic length. For short plasma length, the electrons are mainly accelerated along the laser propagation direction by the combined effect of the oscillating Lorentz force and restoring electrostatic field due to the plasma ions [24,25]. If the laser intensity is sufficiently high and the plasma gradient not too steep, plasma waves can be resonantly excited in the overdense target by the Lorentz force, leading to absorption enhancement [26]. Yet, when the preplasma becomes larger, stochastic heating by the standing electromagnetic wave eventually dominates [29], yielding the maximum absorption rate and the hottest electrons. Although the electrostatic accelerating field in this heating regime is slightly nonuniform, the protons reach higher kinetic energy when such a large preplasma is present in front of the target.

This study suggests that, in the proposed two-pulse setup, the delay between the laser pulses should be just below the transit time of the shock wave through the target. This would maintain a sharp gradient at the target rear surface and allow maximum extension (over distances of several μm) of the front surface plasma, thereby optimizing electron heating and proton acceleration.

3. Dependence of acceleration on pulse duration

Alternatively, optimization of ion energy for a fixed incident laser energy can be obtained by varying the laser parameters, and chiefly its pulse duration. Indeed, one can imagine that a very short and intense pulse would generate a relatively small number of very energetic electrons. On the contrary, we could expect a large number of less energetic electrons from a lower-intensity, longer-duration pulse. How the acceleration varies between these two limits is still a relatively open question. In addition, effects such as variations of the absorption with laser intensity or target

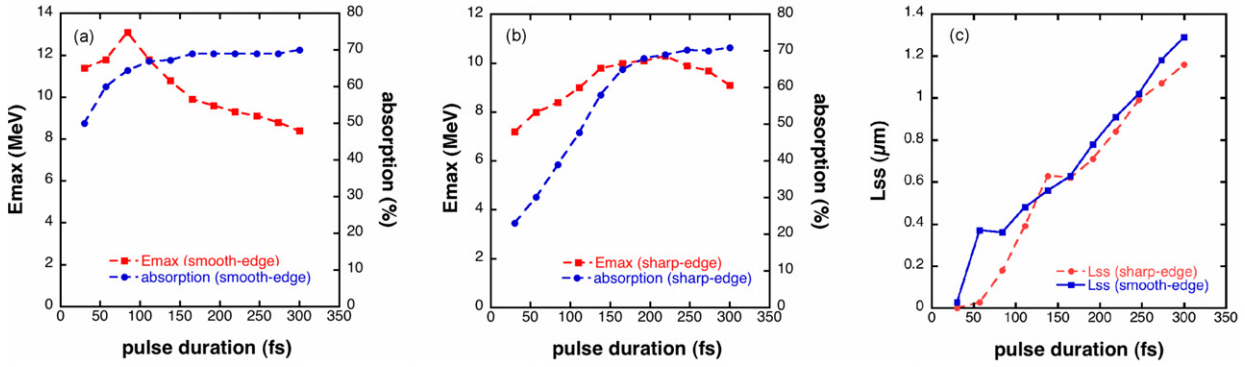

Fig. 2. Maximum proton energy and absorption vs pulse duration for the smooth-edge (a) and sharp-edge (b) target profiles. (c) Gradient length at rear surface, at peak of pulse, vs pulse duration.

preheating by the rising edge of the pulse can affect the position of the optimum pulse duration for the maximum proton energy between these two limits.

We show in this section that varying the pulse duration actually influences the maximum proton energy through three mechanisms: the characteristic gradient length at the target rear surface, the characteristic time of energy exchange between protons and electrons, and the laser absorption rate. Overall, we observe relatively moderate variations of the peak proton energy. This weak dependance, however, is found to result from strong but conflicting variations of the above-mentioned parameters.

3.1. Numerical results

In order to study the effect of pulse duration on the maximun proton energy, we carried out another set of 2D simulations using CALDER. In these simulations, the p-polarized laser pulse with a wavelength of 0.8 μm is emitted from the left side of the simulation box with an incidence angle of 45° on target and a focal spot of 2.8 μm. The pulse temporal and spatial profiles are Gaussian. The temporal full width at half maximum, τ_p, is varied from 30 fs to 300 fs. The pulse energy is kept constant and equal to 0.14 J. Consequently, its intensity varies from 3.6×10^{19} W/cm^2 to 3.6×10^{18} W/cm^2. The peak intensity enters the box at a time equal to 1.83 times the FWHM, so that the rising edge of the main pulse can be fully described. In our simulations, we used either a sharp-edge or a smooth-edge target, the latter with an exponential preplasma at the front side of the form

$$n_e(x) = 50 n_c \times \exp\left(\frac{-x}{l_{ss}}\right)$$

l_{ss} is the characteristic gradient length and the preplasma density therefore goes from 1% to 100% of $50n_c$ over $4.6l_{ss}$. The target is fully-ionized hydrogen. The numerical parameters and boundary conditions used are similar to those of the previous section.

All simulations have been run to roughly 600 fs after the peak of the laser pulse reaches the target front surface, a point where we are confident that subsequent evolution of ion peak energy will not qualitatively change our conclusions. For all the pulse durations we considered, we plot in Figs. 2a) and 2b) the maximum proton energy at $t = 500$ fs and the absorption as a function of pulse duration, τ_p. For both target profiles, we notice a steady increase of absorption with pulse duration: from 50% for $\tau_p = 30$ fs to 70% for $\tau_p = 300$ fs for the smooth-edge target, and even larger variations for the sharp-edge target, from 22% for the shortest pulses to 70% for the longest ones. In comparison, the variations of the maximum proton energy are more subtle. For smooth-edge targets, it first increases slightly from 11 to 13 MeV between $\tau_p = 30$ fs and 84 fs, then decreases down to 8 MeV as the pulse duration becomes longer. A similar trend is observed for the other target profile, but the peak proton energy now only reaches roughly 10 MeV at $\tau_p = 219$ fs before decreasing for larger pulse durations.

3.2. Discussions

During the rising edge of the pulse, significant electron heating starts around $\sim 10^{17}$ W/cm^2 and the hot electrons expand around the target. When the laser pulse duration increases, the front surface plasma heated by the rising edge of the pulse has more time to expand before the peak intensity hits the target. As the electron density gradient length increases at the front side, absorption increases [32,19] and more electrons are heated to high temperature. This effect is more apparent for the sharp-edge targets, for which no preplasma is initially present. These heated electrons travel through the target, come out at the rear side and expand into the vacuum, creating an electrostatic field which starts accelerating protons located at the back surface. Thus, protons begin to be accelerated before the arrival of the peak of the pulse at the target front surface. This early proton acceleration creates a density gradient expanding from the back surface into vacuum. This gradient is known to diminish the strength of the electrostatic field seen by the protons located at the back surface [22,33]. In Fig. 2c), the back surface gradient length at the time of peak intensity is plotted as a function of the laser pulse duration for both target profiles. It can be seen that the gradient length increases with τ_p. This is related to the expansion time of protons which becomes larger when the laser pulse duration increases.

This gradient created at the rear side should hamper proton acceleration [22]. However one can notice from Figs. 2a) and 2b) that the maximum proton energy first increases with τ_p before decreasing. We are actually facing a competition between absorption, screening by the rear side density gradient, and variations in the characteristic energy exchange time between electrons and protons. While the gain in proton energy due to absorption is higher than the loss due to electrostatic shielding at the rear surface, the maximum proton energy increases. On the contrary, when the energy gain due to absorption cannot overcome the loss due to shielding anymore, we observe a decrease in the maximum proton energy. This balance points out to the existence of an optimum pulse duration. This optimum is found to be relatively weak, and depends on the details of the interaction: for instance, it varies from 84 fs to 219 fs when the target profile is changed from smooth-edge to sharp-edge in the above calculations.

3.3. Conclusion

In this study of pulse duration influence on ion acceleration, as well as more detailed analyses that will be published elsewhere [18], we identified three processes through which a variation of pulse duration influences the maximum proton energy: the preplasma expansion at the front side of the target [17], the early rear side expansion due to electron heating before the arrival of the pulse peak, and the acceleration time. We have shown that despite strong variations of each of these parameters, they eventually combine to result in relatively moderate variations of the peak proton energy as a function of pulse duration.

4. Isochoric heating with protons

To ensure uniform ion energy deposition through a thin target, it is possible to take advantage of the variations of the proton stopping power with energy. Ions are known to deposit their energy more efficiently towards the end of their range, in the so-called Bragg peak, whereas the stopping power variations at high energy are relatively moderate. A palatable idea is then to tailor the accelerated ion distribution in order to suppress low-energy protons and make sure that all protons incident on the second target are energetic enough to be transmitted through it with little variations of their stopping power along the target thickness. Modification of the proton spectrum has been predicted or observed to result from a variation of the deposited proton layer at the target rear surface, from a variation of the proton doping fraction in multi-ion species targets [34], and from a variation of the proton layer radius when 2D geometry effects are concerned. We will review below the effect of these parameters.

4.1. Proton acceleration

We will first use the CALDER code to compute proton acceleration in 2D geometry off a thin, dense target, with various types of proton layers deposited on its back surface. In all these calculations, the incident laser pulse has a 0.8 μm wavelength, is linearly polarized and incident from the lower left corner of the simulation box in p polarization, with an angle of 45° on target. The pulse duration is 65 fs full width at half maximum (FWHM) and the focal spot diameter is 8 μm FWHM. The normalized laser field amplitude is $a_0 = 1.6$, corresponding to an intensity of

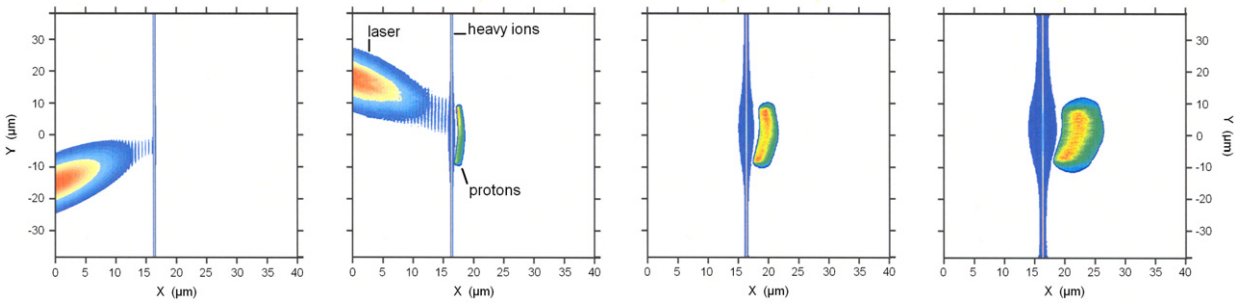

Fig. 3. Laser intensity and ion densities (heavy ions and protons) throughout the simulation at $t = 93$, 245, 361, and 513 fs.

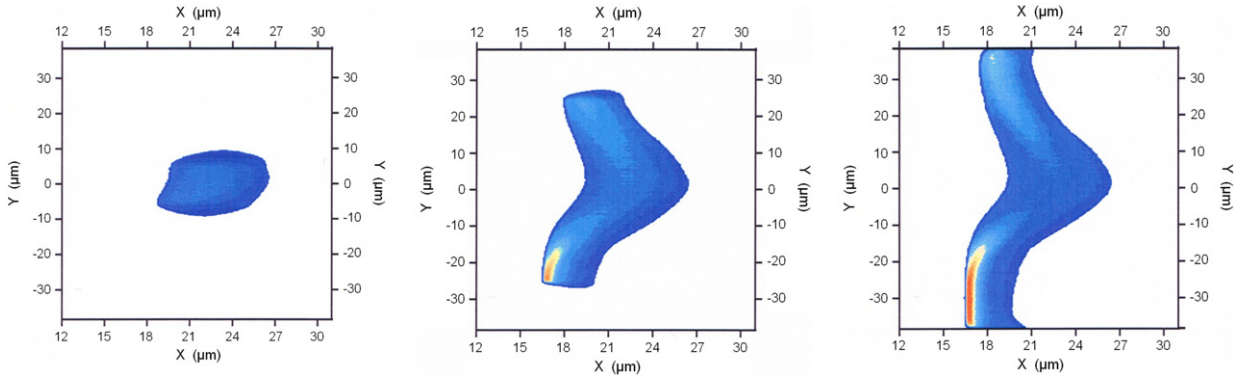

Fig. 4. Proton bunch densities at the end of the simulations ($t = 513$ fs) for three initial proton layer diameters: 13, 51, and 77 μm. (The top of the color scale is at $0.1 n_c$.) The initial proton layer position is $x = 16.4$ μm.

5.5×10^{18} W/cm^2. This laser pulse is incident onto a 140 nm-thick, 100 n_c bulk target, with an ion mass-to-charge ratio equal to ten times that of protons.

In a first series of simulations, we considered a proton layer of 10 nm thickness at the back surface of this target, with a density of 10 n_c, and varied its radial extent between 13, 18, 51, and 77 μm – the latter value being equal to the whole transverse dimension of the simulation box. In a second series of simulations, we kept the diameter of the proton layer equal to 18 μm, but varied instead its density, from 5 to 50 n_c. In a last simulation, the proton layer was replaced by a homogeneous mixture of heavy ions and protons throughout the whole target, with a 1% fraction of protons.

The simulation setup and geometry are illustrated in the first panel of Fig. 3, where the incident laser pulse and target ion densities are superimposed early in the simulation, at $t = 93$ fs. The incident pulse has barely reached the solid target and the proton layer cannot be distinguished from the heavy substrate. Later on, in the second panel taken at $t = 245$ fs, the incident laser pulse has been fully reflected or absorbed, and the protons have moved within 2 μm from their initial location. In the last two panels, at 361 and 513 fs, the proton layer becomes fully detached from the substrate, as all protons become accelerated to finite energy. The layer becomes thicker and less dense as it accelerates, because the accelerating field is not uniform longitudinally throughout the layer. It also picks up some curvature, due to a similar transverse inhomogeneity.

When the proton layer diameter and density are varied, the parameters of the accelerated proton bunch can change drastically. The shapes of the proton bunch at the end of the simulations for three diameters are plotted in Fig. 4. Relatively homogeneous acceleration can be given to layers that are transversely limited to a few times the incident laser spot. For larger dimensions, the transverse variations of the accelerating field lead to strong inhomogeneities in the proton bunch, with some particles located more than 20 μm from the center of the target that can be barely accelerated. This difference is even more visible when the proton layer initially extends across the whole target rear surface. Its outer edges are then clearly unable to detach from the substrate, whereas all the protons located just behind the laser impact on target are accelerated to more than 1 MeV. Note that the slight top–down asymmetry in Figs. 3

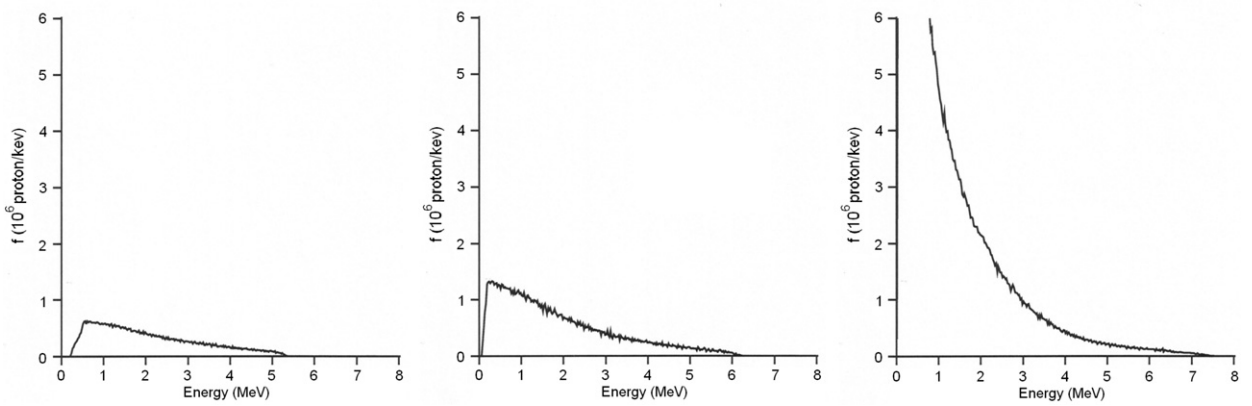

Fig. 5. Proton energy distributions at the end of the simulations ($t = 513$ fs) for three initial proton layer densities: 5, 10, and 50 n_c.

and 4 can be attributed to the imperfect vertical alignment between the center of the proton layer, the center of the simulation box, and the laser impact on target.

Consistent with these observations, the proton energy distributions for the wide or dense layers show broad spectra extending up to zero kinetic energy, where a maximum number of particles are located. On the other hand, for small enough layers (13 and 18 μm diameters) as well as for the lower proton layer densities (5 and 10 n_c), a non-zero minimum cutoff energy is observed, and the position of this cutoff is found to increase when thinner or less dense proton layers are used. This trend is clearly apparent in the three panels of Fig. 5 where the distributions are compared for a 18 μm diameter layer at 5, 10, and 50 n_c density. But one also observes that as the minimum energy cutoff moves to higher values, the overall number of protons at a given energy is also reduced. In other words, using thinner and thinner proton layer densities enables to produce proton bunches without the low-energy particles that are detrimental for uniform energy deposition, but at the same time this acceleration is less and less efficient.

Finally, let us mention that if the last target type, in which the protons are uniformly distributed inside the substrate initially, does indeed lead to a spectrum showing some modulations as previously reported [34], the overall efficiency and high-energy particle numbers are even lower, and a large amount of low-energy protons can still be observed, suggesting that this type of targets is not appropriate for heating experiments without due optimization.

4.2. Heating of a thin aluminum layer

The canonical secondary target that we consider below is a 10 μm aluminum target, a case already considered experimentally. The front surface of this target is separated by 246 μm of vacuum from the back of the laser-irradiated, proton-producing target. We use here the CMC particle transport code to compute the propagation and slowing-down of protons in this solid target, and the energy they deposit along their paths. This code and the stopping powers it uses have been documented in a previous publication [16]. The self-consistent evolution of stopping powers as a function of target heating and ionization is not accounted for here: only the "cold" stopping powers for aluminum are used [35]. Protons accelerated in the CALDER PIC calculations are input in the CMC calculation with their specific positions and momenta. Their trajectories are then followed until they hit the target, slow down and deposit part of their kinetic energy in the aluminum layer. Typical proton trajectories and a map of the resulting deposited energy are plotted in Fig. 6a), corresponding to the above PIC calculation with a 10 n_c, 18 μm diameter proton layer at the back surface of the laser-irradiated target. High energy protons arrive first on target and are energetic enough to be rapidly transmitted. Therefore, energy deposition at the front and rear target surfaces initially follow similar variations. Later on, as lower-energy protons reach the secondary target, these particles are not energetic enough to be transmitted through the target. Therefore, the front and rear surface specific energies are decoupled, with the front surface being heated for several more picoseconds by low-energy protons. This trend is apparent in Fig. 6b), where the variations of specific energies with time are plotted for the peak value across the target, and two points close to the laser axis on the front and rear surfaces.

With little surprise, we observe that similar coupled calculations for lower-density proton layers, as considered in Fig. 5, lead to less decoupling between the target front and rear surfaces, as less low-energy protons are present in

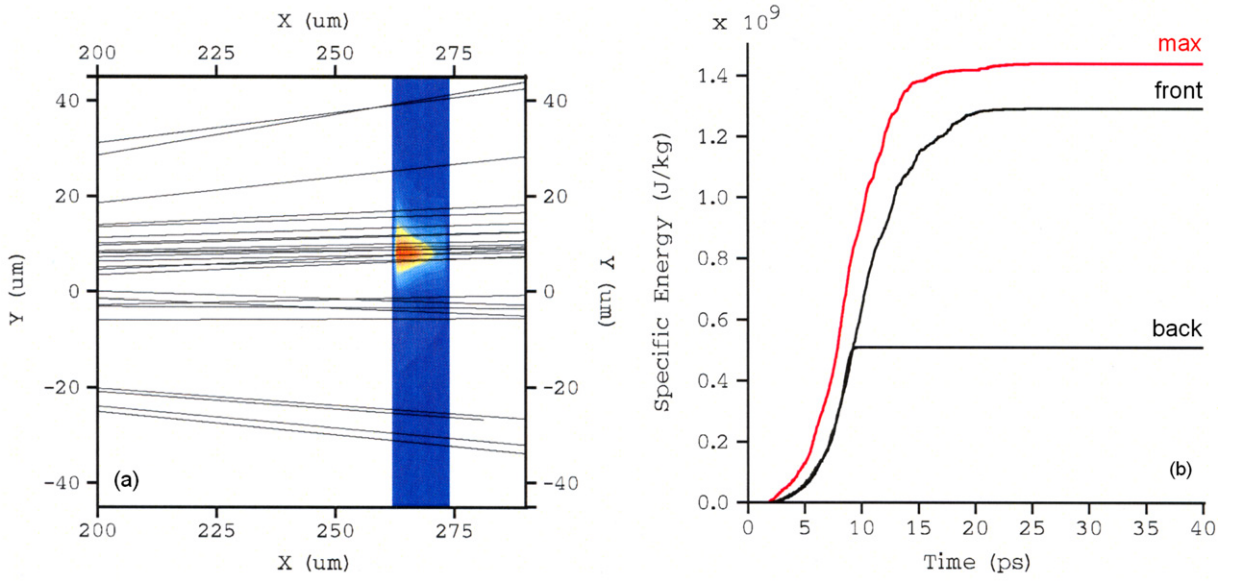

Fig. 6. (a) Trajectories of protons emitted by the laser-irradiated target (not shown), that propagate from its back surface and heat the secondary aluminum target; the color code indicates the specific energy deposited in the target; (b) Specific energy deposited in the aluminum layer by the incident proton beam. Peak value (red) and values on two points at the front and back target surfaces.

the incident beam. For instance, the ratio of front to back surface specific energies is $E_{\text{front}}/E_{\text{back}} \simeq 2.5$ in Fig. 6b), obtained for a 10 n_c, 18 μm diameter proton layer at the first target back surface. This ratio increases to $E_{\text{front}}/E_{\text{back}} > 4$ for a 20 n_c layer, and decreases to roughly 2 for a 5 n_c layer. However, as the mismatch between front and rear surfaces is reduced with lower layer densities, so is also the absolute value of specific energy, as less protons are incident on the secondary target.

5. Conclusions

Proton acceleration from the rear surface of thin laser-irradiated solid foils depends on a number of parameters such as target density profile and thickness, laser intensity, energy, pulse duration, polarization and angle of incidence. The intricacies of these dependences only begin to be elucidated. Two strategies for optimizing the peak proton energy were followed in this article. We first showed that under certain conditions, a controlled low-intensity prepulse could be helpful by preforming a smooth density profile at the irradiated surface of the target and hence increasing the high-intensity laser absorption. Our calculations suggest that the maximum delay between the low- and high-intensity pulses should be used that is compatible with an unperturbed target back surface. Alternatively, lengthening the high-intensity pulse duration, even if it comes at the expense of its peak intensity, may also increase the peak proton energy as the early part of the pulse heats up the front target surface and increases the absorption of the trailing part. Some optimum pulse duration can be found for which this effect dominates the reduction of proton energy due to screening of the back surface electrostatic field by the density gradient that also develops there.

Some preliminary calculations of heating by these laser-produced proton beams were finally reported. They showed that a low-energy cutoff can be created in the proton distribution by reducing the proton layer radius and density, albeit at the expense of the overall acceleration efficiency. Proton layers that are either too thick or larger than a few times the laser spot radius lead to proton distributions that show no low-energy cutoff and therefore result in very non-uniform energy deposition in the secondary target. On the other hand, using properly optimized proton-producing targets irradiated with typical 30 fs laser pulses at a few Joule level, one should be able to heat aluminum to GJ/kg specific energy with interesting uniformity across 5 μm-thick samples.

References

[1] V. Yanovsky, V. Chvykov, G. Kalinchenko, P. Rousseau, T. Planchon, T. Matsuoka, A. Maksimchuk, J. Nees, G. Chériaux, G. Mourou, K. Krushelnick, Opt. Express 16 (2008) 2109.

[2] T.E. Cowan, J. Fuchs, H. Ruhl, A. Kemp, P. Audebert, M. Roth, R. Stephens, I. Barton, A. Blazevic, E. Brambrink, J. Cobble, J. Fernández, J.-C. Gauthier, M. Geissel, M. Hegelich, J. Kaae, S. Karsch, G.P. Le Sage, S. Letzring, M. Manclossi, S. Meyroneinc, A. Newkirk, H. Pépin, N. Renard-LeGalloudec, Phys. Rev. Lett. 92 (2004) 204801.

[3] J. Fuchs, T.E. Cowan, P. Audebert, H. Ruhl, L. Gremillet, A. Kemp, M. Allen, A. Blazevic, J.-C. Gauthier, M. Geissel, M. Hegelich, S. Karsch, P. Parks, M. Roth, Y. Sentoku, R. Stephens, E.M. Campbell, Phys. Rev. Lett. 91 (2003) 255002.

[4] M. Borghesi, D.H. Campbell, A. Schiavi, M.G. Haines, O. Willi, A.J. MacKinnon, P. Patel, L.A. Gizzi, M. Galimberti, R.J. Clarke, F. Pegoraro, H. Ruhl, S. Bulanov, Phys. Plasmas 9 (2002) 2214.

[5] P.K. Patel, A.J. Mackinnon, M.H. Key, T.E. Cowan, M.E. Foord, M. Allen, D.F. Price, H. Ruhl, P. Springer, R. Stephens, Phys. Rev. Lett. 91 (2003) 125004.

[6] S.V. Bulanov, V.S. Khoroshkov, Plasma Phys. Rep. 28 (2002) 453.

[7] M. Roth, T.E. Cowan, M.H. Key, S.P. Hatchett, C. Brown, W. Fountain, J. Johnson, D.M. Pennington, R.A. Snavely, S.C. Wilks, K. Yasuike, H. Ruhl, F. Pegoraro, S.V. Bulanov, E.M. Campbell, M.D. Perry, H. Powell, Phys. Rev. Lett. 86 (2001) 436.

[8] B.M. Hegelich, B.J. Albright, J. Cobble, K. Flippo, S. Letzring, M. Paffett, H. Ruhl, J. Schreiber, R.K. Schulze, J.C. Fernández, Nature 439 (2006) 441.

[9] H. Schwoerer, S. Pfotenhauer, O. Jäckel, K.-U. Amthor, B. Liesfeld, W. Ziegler, R. Sauerbrey, K.W.D. Ledingham, T. Esirkepov, Nature 439 (2006) 445.

[10] T. Toncian, M. Borghesi, J. Fuchs, E. d'Humières, P. Antici, P. Audebert, E. Brambrink, C.A. Cecchetti, A. Pipahl, L. Romagnani, O. Willi, Science 312 (2006) 410.

[11] A.P.L. Robinson, D. Neely, P. McKenna, R.G. Evans, Plasma Phys. Controlled Fusion 49 (2007) 373.

[12] N. Kumar, A. Pukhov, Phys. Plasmas 15 (2008) 053103.

[13] P. Antici, J. Fuchs, S. Atzeni, A. Benuzzi, E. Brambrink, M. Esposito, M. Koenig, A. Ravasio, J. Schreiber, A. Schiavi, P. Audebert, J. Phys. IV France 133 (2006) 1077.

[14] R.A. Snavely, B. Zhang, K. Akli, Z. Chen, R.R. Freeman, P. Gu, S.P. Hatchett, D. Hey, J. Hill, M.H. Key, Y. Izawa, J. King, Y. Kitagawa, R. Kodama, A.B. Langdon, B.F. Lasinski, A. Lei, A.J. MacKinnon, P. Patel, R. Stephens, M. Tampo, K.A. Tanaka, R. Town, Y. Toyama, T. Tsutsumi, S.C. Wilks, T. Yabuuchi, J. Zheng, Phys. Plasmas 14 (2007) 092703.

[15] M.E. Foord, P.K. Patel, A.J. Mackinnon, S.P. Hatchett, M.H. Key, B. Lasinski, R.P.J. Town, M. Tabak, S.C. Wilks, High Energy Density Phys. 3 (2007) 365.

[16] E. Lefebvre, E. d'Humières, S. Fritzler, V. Malka, J. Appl. Phys. 100 (2006) 113308.

[17] R. Nuter, L. Gremillet, P. Combis, M. Drouin, E. Lefebvre, A. Flacco, V. Malka, J. Appl. Phys. 104 (2008) 103307.

[18] M. Carrié, E. Lefebvre, A. Flacco, V. Malka, in preparation.

[19] E. Lefebvre, G. Bonnaud, Phys. Rev. E 55 (1997) 1011.

[20] E. Lefebvre, N. Cochet, S. Fritzler, V. Malka, M.-M. Aléonard, J.-F. Chemin, S. Darbon, L. Disdier, J. Faure, A. Fedotoff, O. Landoas, G. Malka, V. Méot, P. Morel, M. Rabec Le Gloahec, A. Rouyer, Ch. Rubbelynck, V. Tikhonchuk, R. Wrobel, P. Audebert, C. Rousseaux, Nucl. Fusion 43 (2003) 629.

[21] J.-P. Colombier, P. Combis, A. Rosenfeld, I.V. Hertel, E. Audouard, R. Stoian, Phys. Rev. B 74 (2006) 224106.

[22] A.J. Mackinnon, M. Borghesi, S. Hatchett, M.H. Key, P.K. Patel, H. Campbell, A. Schiavi, R. Snavely, S.C. Wilks, O. Willi, Phys. Rev. Lett. 86 (2001) 1769.

[23] T.-Y. Brian Yang, W.L. Kruer, R.M. More, A.B. Langdon, Phys. Plasmas 2 (1995) 3146.

[24] P. Gibbon, E. Förster, Plasma Phys. Controlled Fusion 38 (1996) 769.

[25] P. Mulser, D. Bauer, H. Ruhl, Phys. Rev. Lett. 101 (2008) 225002.

[26] A.A. Andreev, K.Yu. Platonov, T. Okada, S. Toraya, Phys. Plasmas 10 (2003) 220.

[27] Z.-M. Sheng, K. Mima, Y. Sentoku, M.S. Jovanović, T. Taguchi, J. Zhang, J. Meyer-ter-Vehn, Phys. Rev. Lett. 88 (2002) 055004.

[28] A. Bourdier, D. Patin, E. Lefebvre, Physica D 206 (2005) 1.

[29] Y. Sentoku, V.Y. Bychenkov, K. Flippo, A. Maksimchuk, G. Mourou, Z.M. Sheng, D. Umstadter, Appl. Phys. B 74 (2002) 207.

[30] H. Ruhl, A. Macchi, P. Mulser, F. Cornolti, S. Hain, Phys. Rev. Lett. 82 (1999) 2095.

[31] Y. Oishi, T. Nayuki, T. Fujii, Y. Takizawa, X. Wang, T. Yamazaki, K. Nemoto, T. Kayoiji, T. Sekiya, K. Horioka, Y. Okano, Y. Hironaka, K.G. Nakamura, K. Kondo, A.A. Andreev, Phys. Plasmas 12 (2005) 073102.

[32] S. Wilks, W. Kruer, M. Tabak, A.B. Langdon, Phys. Rev. Lett. 69 (1992) 1383.

[33] T. Grismayer, P. Mora, Phys. Plasmas 13 (2006) 032103.

[34] A.P.L. Robinson, A.R. Bell, R.J. Kingham, Phys. Rev. Lett. 96 (2006) 035005.

[35] J.F. Ziegler, J. Appl. Phys. 85 (1999) 1249.